Phase-Lifting Extended State Observer-Based Switching Quasiresonant Control Design for PMSMs With Periodic and Aperiodic Disturbances

Jinlin Sun, *Member, IEEE*, Nengwen Zhu, Qiankang Hou, Shihong Ding, *Senior Member, IEEE*, and Jun Yang, *Fellow, IEEE*

***Abstract*—Achieving robust and precise speed regulation in permanent magnet synchronous motor (PMSM) drive systems remains a significant challenge, particularly under disturbances comprising both periodic and aperiodic components. For aperiodic disturbances, disturbance observers are commonly employed; however, conventional designs often exhibit slow convergence and phase lag, limiting their effectiveness. To address the issue of slow convergence, we first develop a modified supertwisting extended state observer (MSESO), which guarantees finite-time convergence while avoiding the discontinuities inherent in traditional sliding mode observers. Building upon the MSESO, a phase-lifting extended state observer is further designed to mitigate phase lag and enhance the dynamic performance of disturbance estimation. Its phase-lifting characteristics are quantitatively validated via frequency-domain analysis. To suppress periodic disturbances, a switching quasiresonant (SQR) controller is developed, which demonstrates superior harmonic rejection capability. In contrast to conventional quasiresonant controllers that may degrade system dynamics, the proposed SQR controller employs a smooth switching mechanism to activate resonant compensation only when needed, thereby preserving transient performance. Extensive experimental results under both aperiodic and periodic disturbance conditions demonstrate that the proposed control scheme achieves robust disturbance rejection and high steady-state speed accuracy in PMSMs.**

***Index Terms*—Active disturbance rejection control (ADRC), aperiodic and periodic disturbances, permanent magnet synchronous motor (PMSM), sliding mode control, speed regulation.**

I. INTRODUCTION

THE accuracy and reliability of speed control in permanent magnet synchronous motor (PMSM) systems are crucial for a wide range of industrial applications [1], [2], [3], [4], [5], including robotics, electric vehicles, and high-performance servosystems. However, the speed control loop is susceptible to performance degradation due to both periodic and aperiodic disturbances. These disturbances can generally be classified into two types: periodic disturbances [6], [7], [8], such as those caused by electrical harmonics, mechanical vibrations, and inverter nonlinearities; and aperiodic disturbances, including sudden load changes or external influences. Such disturbances can induce speed fluctuation, torque ripple, and instability, ultimately degrading the overall performance of PMSMs.

In response to the challenges posed by aperiodic disturbances in PMSM systems, speed controllers are commonly designed to mitigate their adverse effects, with proportional–integral (PI) controllers being the most widely adopted in industrial applications due to their simplicity and ease of implementation [9]. However, the performance of PI controllers degrades significantly in the presence of time-varying operating conditions. Specifically, their ability to reject aperiodic disturbances deteriorates in such environments, limiting their suitability for high-performance PMSM applications [10].

To achieve effective rejection of aperiodic disturbances in PMSM systems, various advanced control strategies have been proposed in recent years. These include sliding mode control [11], [12], [13], [14], model predictive control, active disturbance rejection control (ADRC) [15], [16], and adaptive neural network control. Among these methods, ADRC has attracted widespread attention due to its distinctive advantages. The core strength of this approach lies in its ability to achieve effective control without relying on an accurate system model, thereby ensuring robust performance against both internal uncertainties and external disturbances [17], [18]. Specifically, ADRC adopts an innovative approach that integrates internal uncertainties and external disturbances into a unified total disturbance. Based on this formulation, ADRC enables real-time estimation and dynamic compensation of the total disturbance, thereby significantly enhancing the robustness and transient performance of PMSM speed control under aperiodic disturbances.

Received 5 August 2025; revised 13 October 2025 and 25 December 2025; accepted 9 January 2026. Date of publication 13 January 2026; date of current version 20 March 2026. This work was supported in part by the National Natural Science Foundation of China under Grant 62203189, Grant 62573212, Grant 62373170, and Grant 62403079, in part by the 10th Young Elite Scientists Sponsorship Program by CAST, in part by the China Postdoctoral Science Foundation under Grant 2024M751187, and in part by the Natural Science Foundation of Jiangsu Province under Grant BK20240963. Recommended for publication by Associate Editor X. Zhang. *(Corresponding author: Shihong Ding.)*

Jinlin Sun, Nengwen Zhu, and Shihong Ding are with the School of Electrical and Information Engineering, Jiangsu University, Zhenjiang 212013, China (e-mail: jsun@ujs.edu.cn; zhunengwen@stmail.ujs.edu.cn; dsh@ujs.edu.cn).

Qiankang Hou is with the School of Mechanical Engineering and Rail Transit, Changzhou University, Changzhou 213164, China (e-mail: hqk@cczu.edu.cn).

Jun Yang is with the Department of Aeronautical and Automotive Engineering, Loughborough University, LE11 3TU Loughborough, U.K. (e-mail: j.yang3@lboro.ac.uk).

Color versions of one or more figures in this article are available at https://doi.org/10.1109/TPEL.2026.3653900.

Digital Object Identifier 10.1109/TPEL.2026.3653900

At the core of the ADRC framework lies the extended state observer (ESO), which is responsible for estimating both the system states and the total disturbance in real time [19]. For PMSM speed control subject to aperiodic disturbances, the ESO plays a central role in disturbance rejection by enabling dynamic compensation of total internal uncertainties and external perturbations. In [20], a linear extended state observer (LESO) is applied to motor speed control, adopting a bandwidth-based design to simplify implementation and parameter tuning. However, achieving satisfactory speed control performance with LESO often requires a high observer bandwidth, which in turn amplifies high-frequency measurement noise and may degrade system robustness [21]. To mitigate these issues while preserving structural simplicity, adaptive ESO schemes have been introduced [22]. These methods dynamically adjust observer gains to improve estimation precision under varying operating conditions [23]. Nevertheless, adaptive ESO schemes often suffer from complicated tuning procedures and slower convergence speed, particularly under rapidly varying aperiodic disturbances and strongly nonlinear conditions. Thus, in PMSM speed control applications, designing an ESO that simultaneously ensures fast convergence and strong robustness remains a key objective for achieving high-performance aperiodic disturbance rejection capability.

To improve the convergence speed of ESOs under aperiodic disturbances, sliding mode algorithms have been introduced into observer design [24], [25]. Among them, the supertwisting sliding mode algorithm has been widely used to construct the supertwisting ESO (SESO), which ensures finite-time convergence and strong robustness [26], [27], [28], [29]. The SESO mitigates the chattering associated with classical sliding mode control by transferring the discontinuous action to higher order derivatives and incorporating integral terms [30], [31], [32]. However, the SESO still involves discontinuities within its integral structure. Although the SESO can mitigate chattering, it cannot completely eliminate this phenomenon, often leading to residual oscillations and compromised estimation accuracy [33]. To address this issue, some improved SESO schemes have been proposed [34], [35], including the continuous SESO in [36] and [37], which replaces discontinuities with smooth approximations. While these continuous observers reduce chattering, they sacrifice finite-time convergence and introduce additional phase lag. Such limitations hinder observer performance in dynamic environments with rapidly varying disturbances, motivating the development of enhanced observers that maintain finite-time convergence while improving phase characteristics.

In addition to challenges in observer design, ADRC exhibits limited effectiveness in suppressing periodic disturbances in PMSM systems, which can significantly degrade steady-state speed performance. Although ESOs improve the real-time estimation of aperiodic components, they exhibit limited capability in handling periodic ones, ultimately constraining the overall disturbance rejection performance of ADRC [38]. To overcome this limitation, several hybrid control strategies have been proposed. These strategies integrate ADRC with other techniques, such as resonant control, repetitive control, and iterative learning control (ILC) [39]. For example, ADRC-ILC frameworks have demonstrated improved performance in rejecting periodic disturbances in high-precision PMSM speed regulation [40]. However, these approaches often introduce increased computational burden, complex parameter tuning, and degraded dynamic responsiveness due to the use of auxiliary control loops. Therefore, designing a control strategy that effectively suppresses periodic disturbances in PMSM systems while maintaining simple structure and preserving dynamic response performance remains a critical challenge.

Motivated by the above-mentioned challenges, this article proposes a novel phase-lifting extended state observer (PLESO)-based switching quasiresonant (SQR) control scheme for PMSM systems. The uniqueness of this work lies in the development of a control scheme specifically designed to address both periodic and aperiodic disturbances in PMSM speed regulation. Compared with existing works, the main novelties and contributions of this article are summarized as follows.

1) By embedding a constrained command filter into the supertwisting algorithm framework, the proposed PLESO provides phase-lifting compensation and substantially enhances the transient response, thereby mitigating the limited disturbance estimation capability typical of conventional ESOs [41], [42].
2) Unlike existing finite-time observer designs [43], [44], the proposed PLESO attains finite-time convergence without employing discontinuous nonlinearities (e.g., the sign function), thereby suppressing chattering and improving steady-state estimation accuracy.
3) Compared with conventional quasiresonant (QR) controllers [45], [46], which activate the resonant loop via abrupt switching and can degrade transient performance, the proposed SQR controller implements a smooth switching mechanism that preserves the PMSM dynamic speed response under periodic disturbances.

The rest of this article is organized as follows. Section II briefly introduces the PMSM system model and the conventional LESO design. Section III details the proposed PLESO-based SQR control scheme. Section IV presents experimental results that validate the effectiveness of the proposed control scheme. Finally, Section V concludes this article.

II. MATHEMATICS MODEL AND PROBLEM FORMULATION

A. Mathematical Model of PMSM Systems With Disturbances

In the d-q reference frame, the dynamic model of a PMSM is described as

$$J\dot{\omega}_m = T_e - B\omega_m - T_L \tag{1}$$

where ω_m represents the mechanical angular speed, B is the viscous friction coefficient, T_e is the electromagnetic torque, J is the inertia of the PMSM, and T_L is the load torque.

For a surface-mounted PMSM with $L_d = L_q$, and under field-oriented control with $i_d = 0$, the electromagnetic torque simplifies to

$$T_e = \frac{3}{2}n_p i_q[i_d(L_d - L_q) + \psi_f] = \frac{3}{2}n_p\psi_f i_q = Ki_q \tag{2}$$

where $K = \frac{3}{2} n_p \psi_f$ is the torque coefficient, n_p is the number of pole pairs, and i_q is the stator current in the q-axis. Substituting (2) into (1) yields the mechanical dynamics

$$\begin{aligned}\dot{\omega}_m &= \frac{K i_q}{J} - \frac{B\omega_m}{J} - \frac{T_L}{J} \\ &= \frac{K i_q^*}{J} - \frac{B\omega_m}{J} - \left(\frac{K i_q^*}{J} - \frac{K i_q}{J}\right) - \frac{T_L}{J} \end{aligned} \tag{3}$$

where i_q^* denotes the reference q-axis current input. The term $\frac{K i_q^*}{J} - \frac{K i_q}{J}$ is the difference between the commanded and actual currents.

The load torque T_L and the PMSM parameters, such as J, may vary over time, and nonideal effects cause additional disturbances. Among these, periodic disturbances mainly originate from stator current sampling errors, including offset and scaling errors. Based on the analysis in [47], these current sampling errors result in first-order and second-order torque ripples, which can be modeled as

$$\begin{aligned}\Delta T_1(t) = {} & \frac{2}{\sqrt{3}} K \sqrt{\Delta i_{as}^2(t) + \Delta i_{as}(t)\Delta i_{bs}(t) + \Delta i_{bs}^2(t)} \\ & \times \cos(\omega_e t + \theta_e) \end{aligned} \tag{4}$$

$$\Delta T_2(t) = \frac{K I(t)}{\sqrt{3}} \left(\frac{K_a - K_b}{K_a K_b}\right) \left[\cos\left(2\omega_e t + \frac{\pi}{3}\right) + \frac{1}{2}\right] \tag{5}$$

where ΔT_1 and ΔT_2 denote the first and second torque harmonics, respectively. $\omega_e = n_p \omega_m$ is the electrical angular speed, θ_e is a constant angle, and I is the amplitude of the phase current. In addition, Δi_{as} and Δi_{bs} represent the dc offset errors of phase A and phase B currents, respectively, while K_a and K_b are the scaling factors of phase A and phase B currents.

Considering these factors, the mechanical dynamics can be expressed as

$$\dot{\omega}_m = \frac{K i_q^*}{J} - \frac{B\omega_m}{J} - \left(\frac{K i_q^*}{J} - \frac{K i_q}{J}\right) - \frac{T_L}{J} + \frac{T_h}{J} \tag{6}$$

where the disturbance torque T_h caused by the current sampling errors is

$$T_h = \Delta T_1(t) + \Delta T_2(t). \tag{7}$$

By defining d_t to denote the total disturbance in the speed loop, the PMSM mechanical dynamics can be further rewritten as

$$\dot{\omega}_m = \frac{K i_q^*}{J} + d_t = K_t i_q^* + d_t \tag{8}$$

where $K_t = \frac{K}{J}$ denotes the angular acceleration coefficient, and $d_t = -\frac{B\omega_m}{J} - (\frac{K i_q^*}{J} - \frac{K i_q}{J}) - \frac{T_L}{J} + \frac{T_h}{J}$ is the total disturbance.

Assumption 1: The total disturbance d_t in system (8) is bounded, and its rate of change is limited by a positive constant $d_{\max}$, such that $|\dot{d}(t)| \leq d_{\max}$.

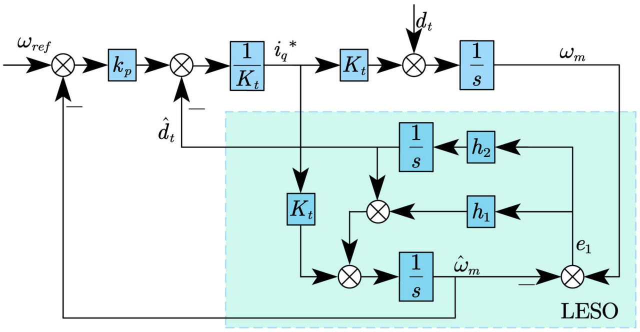

Fig. 1. Conventional ADRC scheme for the PMSM speed regulation system.

B. Conventional ADRC Scheme

To estimate the total disturbance, an LESO is designed for the PMSM system, expressed as

$$\begin{cases}\dot{\hat{\omega}}_m = K_t i_q^* + \hat{d}_t + h_1 e_1 \\ \dot{\hat{d}}_t = h_2 e_1\end{cases} \tag{9}$$

where $\hat{\omega}_m$ and $\hat{d}_t$ denote the estimated motor speed and disturbance, respectively. Here, $e_1 = \omega_m - \hat{\omega}_m$. The observer gains are parameterized as $h_1 = 2\omega_0$ and $h_2 = \omega_0^2$, with ω_0 representing a positive bandwidth-related parameter. Based on the disturbance estimation, the feedback control law can be formulated as

$$i_q^* = \frac{k_p(\omega_{ref} - \hat{\omega}_m) - \hat{d}_t}{K_t} \tag{10}$$

where k_p is the proportional gain. The block diagram of the traditional ADRC system is shown in Fig. 1.

The LESO is widely employed for estimating disturbances and unmodeled dynamics in control systems due to its structural simplicity and ease of implementation. However, its performance remains limited under dynamic operating conditions. The inherent linearity of the LESO results in relatively slow convergence and inadequate robustness against rapidly varying disturbances. Moreover, increasing the observer bandwidth to enhance response speed inevitably amplifies measurement noise. From a frequency-domain perspective, the LESO introduces substantial phase lag in the medium-to-high frequency range, which compromises the accuracy of disturbance estimation and degrades the overall closed-loop performance.

C. Preliminary Concepts and Supporting Lemmas

This section presents the concept of homogeneity and four supporting lemmas essential for proving the main result.

Throughout this article, the notation $\lfloor \cdot \rceil^n$ denotes $|\cdot|^n \operatorname{sign}(\cdot)$, where $n \in \mathbb{R}$.

Definition 1 (See [48]): For $(x_1, \ldots, x_n) \in \mathbb{R}^n$ and real numbers $\delta_i > 0, i = 1, \ldots, n$, a function $V : \mathbb{R}^n \to \mathbb{R}$ is said to be homogeneous of degree τ if there is a real number τ such that for all $\varepsilon > 0$ and all $x \in \mathbb{R}^n \backslash \{0\}$

$$V(\varepsilon^{\delta_1} x_1, \ldots, \varepsilon^{\delta_n} x_n) = \varepsilon^{\tau} V(x_1, \ldots, x_n)$$

with δ_i being called the weights of the coordinates.

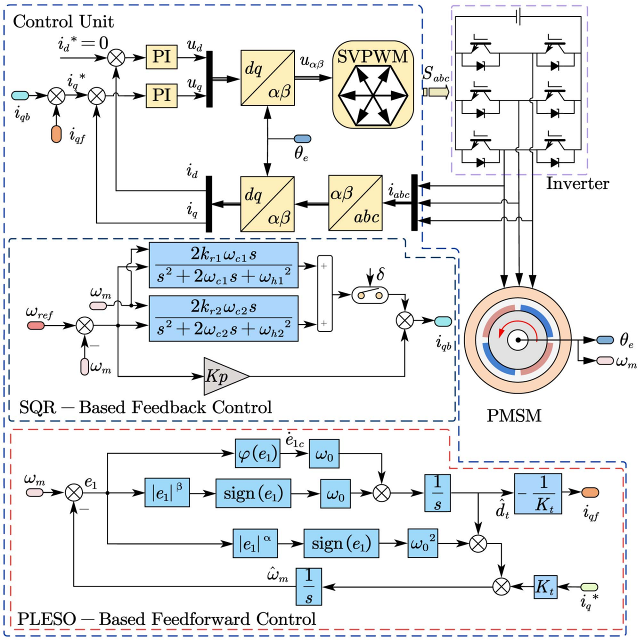

Fig. 2. Block diagram of the proposed control scheme for the PMSM.

Lemma 1 (See [49]): For any $a \geq 1$, one has for all $x, y \in \mathbb{R}$.
1) $|[x]^a - [y]^a| \leq a(2^{a-2}+2)(|x-y|^a + |x-y||y|^{a-1})$.
2) $|[x]^a - [y]^a| \geq 2^{1-a}|x-y|^a$.

Lemma 2 (See [50]): Provided that $0 < b \leq 1$, the following holds for all $x, y \in \mathbb{R}$: $|\lfloor x \rceil^b - \lfloor y \rceil^b| \leq 2^{1-b}|x-y|^b$.

Lemma 3 (See [50]): Let $\varphi(x_1, x_2) > 0$ be a function of x_1 and x_2. For any $c_1, c_2 > 0$, we have

$$|x_1|^{c_1}|x_2|^{c_2} \leq \frac{c_1}{c_1+c_2}\varphi(x_1,x_2)|x_1|^{c_1+c_2} + \frac{c_2}{c_1+c_2}(\varphi(x_1,x_2))^{-\frac{c_1}{c_2}}|x_2|^{c_1+c_2}.$$

Lemma 4 (See [50]): If a function $W(x) : \mathbb{R}^n \to \mathbb{R}$ and a positive-definite function $V(x) : \mathbb{R}^n \to \mathbb{R}$ have the same homogeneous degree with regard to the same dilation weight, then one can find a positive constant $\bar{\rho}$ such that $W(x) \leq \bar{\rho}V(x)$. Furthermore, provided $W(x)$ is positive definite, one can find a positive constant ρ such that $\rho V(x) \leq W(x)$.

III. CONTROL SCHEME DESIGN AND STABILITY ANALYSIS

In this section, we propose the PLESO-based SQR control scheme for the PMSM speed regulation systems. The corresponding design principles and stability analysis are presented in detail. The overall structure of the proposed control scheme is illustrated in Fig. 2, which comprises the PLESO-based feedforward controller and the SQR-based feedback controller. For clarity, in this section, the PLESO refers to the phase-lifting SESO, and the SQR refers to the SQR controller.

A. Design of the PLESO-Based Feedforward Control

To improve convergence speed and enhance robustness under aperiodic disturbance, the SESO is employed. Utilizing the second-order sliding mode structure [51], the SESO ensures finite-time convergence, thereby improving estimation accuracy and dynamic response under aperiodic disturbances. Compared with the LESO given in (9), the SESO provides a faster convergence rate and stronger disturbance rejection capability, while simultaneously reducing steady-state errors. Specifically, the SESO is formulated as

$$\begin{cases} \dot{\hat{\omega}}_m = K_t i_q^* + \hat{d}_t + h_1 \lfloor e_1 \rceil^{0.5} \\ \dot{\hat{d}}_t = h_2 \cdot \mathrm{sign}(e_1). \end{cases} \tag{11}$$

However, the SESO suffers from a significant limitation. The use of the discontinuous sign function $\mathrm{sign}(e_1)$ induces chattering, which excites unmodeled high-frequency dynamics and results in degraded control performance as well as steady-state errors that impair disturbance estimation accuracy. In addition, the inherent discontinuities in the SESO can affect estimation smoothness and robustness when facing rapidly varying and complex disturbances.

To address these issues, a modified supertwisting extended state observer (MSESO) is designed as

$$\begin{cases} \dot{\hat{\omega}}_m = K_t i_q^* + \hat{d}_t + h_1 \lfloor e_1 \rceil^{\alpha} \\ \dot{\hat{d}}_t = h_2 \lfloor e_1 \rceil^{\beta} \end{cases} \tag{12}$$

where $\alpha \in (0.5, 1)$ and $\beta = 2\alpha - 1$. The parameters are defined as $h_1 = 2\omega_0$ and $h_2 = \omega_0^2$, where ω_0 denotes the bandwidth-related parameter of the MSESO.

To evaluate the disturbance rejection performance of different observer-based ADRC schemes, a frequency-sweep method is adopted to generate the Bode diagrams for the PMSM control systems utilizing LESO, SESO, and MSESO. These Bode diagrams are obtained from the speed control loop employing the proportional controller shown in Fig. 1, with the proportional gain set to $k_p = 100$. All observers are configured under a fixed observer bandwidth $\omega_0 = 200$ rad/s; in addition, the MSESO uses $\alpha = 0.75$.

Remark 1: In the frequency-sweep analysis, the total disturbance is modeled as a sinusoidal input $d_t = A_m \sin(\omega_f t)$, where A_m is the disturbance amplitude and ω_f is the disturbance frequency. The PMSM speed response $\omega_m(t)$ reaches a steady-state sinusoidal form $A_f \sin(\omega_f t + \theta_f)$, from which the magnitude and phase responses are calculated as $20\,\lg(A_f/A_m)$ and θ_f, respectively. This approach offers a practical alternative to analytical transfer function derivation [52], enabling empirical construction of Bode diagrams by sweeping the input frequency and measuring steady-state outputs without requiring explicit analytical models.

Fig. 3 presents the Bode diagrams of the LESO, SESO, and MSESO under identical system parameters. The LESO exhibits a linear estimation structure; it is simple but suffers from slow convergence and limited robustness. In addition, the results show that the SESO consistently underperforms relative to the proposed MSESO. In the low- to mid-frequency range, the Bode diagram of the SESO nearly coincides with that of the MSESO, indicating similar phase characteristics when estimating slowly varying disturbances. However, as frequency increases, clear

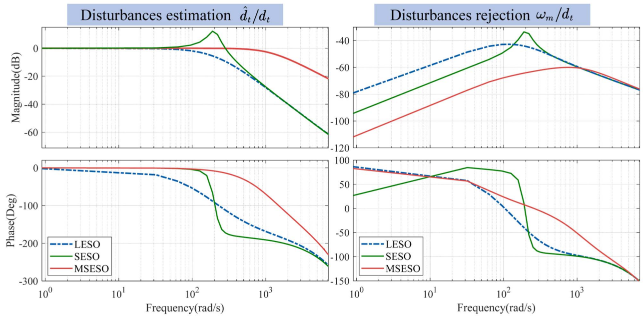

Fig. 3. Bode diagrams of LESO, SESO, and MSESO.

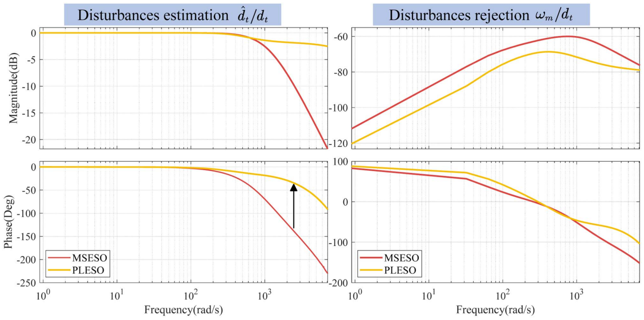

Fig. 5. Bode diagrams of MSESO and PLESO.

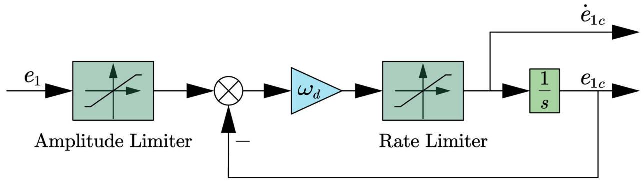

Fig. 4. Constrained command filter of the estimation error e_1.

differences emerge: the SESO's disturbance-estimation transfer function $\hat{d}_t/d_t$ resonates near the bandwidth and exhibits pronounced phase lag beyond the bandwidth. In contrast, the MSESO replaces the discontinuous term with a continuous nonlinear function $\lfloor e_1 \rceil^{\beta}$, reducing chattering and yielding a smoother frequency response with improved disturbance estimation, although it still exhibits noticeable phase lag at high frequencies.

In order to address the phase lag in the disturbance estimation dynamics, we propose incorporating a differential term $\dot{e}_1$ into the observer structure to provide phase lead compensation. However, direct numerical differentiation of e_1 is highly sensitive to measurement noise, which may destabilize the system.

Thus, a constrained command filter is employed to generate a smooth and bounded approximation of $\dot{e}_1$, which eliminates the need for direct numerical differentiation and ensures robustness against high-frequency noise, as illustrated in Fig. 4. The filter is defined by

$$\dot{e}_{1c} = \mathrm{sat}(\omega_d(\mathrm{sat}(e_1, \overline{e_1}, \underline{e_1}) - e_{1c}), \overline{s}, \underline{s}) \tag{13}$$

where e_{1c} is the constrained variable, and ω_d is a positive constant. The saturation bounds $\overline{e_1}$ and $\overline{s}$ define the maximum allowable amplitude and rate, while $\underline{e_1}$ and $\underline{s}$ denote their respective lower limits. The saturation function $\mathrm{sat}(x, \overline{x}, \underline{x})$ is defined as

$$\mathrm{sat}(x, \overline{x}, \underline{x}) = \begin{cases} \overline{x}, & x \geq \overline{x} \\ [4pt] x, & \underline{x} < x < \overline{x} \\ [4pt] \underline{x}, & x \leq \underline{x}. \end{cases} \tag{14}$$

According to [53], the constrained command filter provides an effective approximation of the derivative of e_1, ensures convergence with theoretical guarantees, and behaves like a nonlinear low-pass filter applied to the speed estimation error.

Remark 2: In the constrained command filter (13), the parameter ω_d is tuned to balance the tradeoff between response speed and robustness. Specifically, a larger ω_d increases the tracking speed of the filtered signal $\dot{e}_{1c}$, improving the system's response to rapid variations in the speed estimation error e_1, but may amplify high-frequency noise. Conversely, a smaller ω_d provides smoother filtering at the expense of slower response. Therefore, it is recommended to gradually fine-tune the value of ω_d during experimental trials to achieve balanced performance.

By replacing $\dot{e}_1$ with the filtered signal $\dot{e}_{1c}$, the final form of the PLESO is obtained as

$$\begin{cases} \dot{\hat{\omega}}_m = K_t i_q^* + \hat{d}_t + h_1 \lfloor e_1 \rceil^{\alpha} \\ \dot{\hat{d}}_t = h_2 \lfloor e_1 \rceil^{\beta} + \underbrace{h_3 \dot{e}_{1c}}_{\text{differential term}} \end{cases} \tag{15}$$

where h_3 is a positive constant.

To incorporate the estimated disturbance into the control law, the output of the observer $\hat{d}_t$ is further converted into an equivalent current signal i_{qf}, expressed in amperes, given as

$$i_{qf} = -\frac{\hat{d}_t}{K_t}. \tag{16}$$

Considering Assumption 1, we have that the term $\eta = \dot{d}_t - h_3 \dot{e}_{1c}$ is bounded, i.e., $|\eta| \leq D_{\max}$, where $D_{\max}$ is a positive constant.

To evaluate the dynamic performance of the proposed observer, Fig. 5 presents the frequency-domain analysis comparing the disturbance estimation performance and disturbance rejection performance of the MSESO and PLESO. In disturbance estimation, as characterized by the transfer function $\hat{d}_t/d_t$, the PLESO delivers improved frequency-response magnitude and phase and exhibits greater phase-lifting than the MSESO in the mid-to-high-frequency range. Specifically, the proposed PLESO exhibits a smaller phase lag than the MSESO in the medium- and high-frequency ranges, thereby enhancing the disturbance estimation capability.

Regarding disturbance rejection performance, represented by the transfer function ω_m/d_t, the PLESO exhibits superior performance across the entire frequency range. It not only maintains the robustness and smoothness of the MSESO at low frequencies but also offers stronger rejection capability at higher frequencies. This demonstrates that the phase-lifting design in

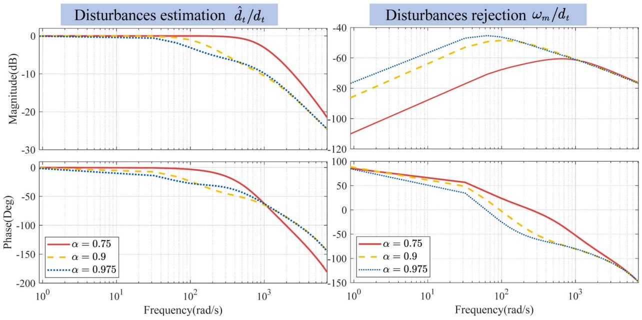

Fig. 6. Bode diagrams of PLESO under different values of α.

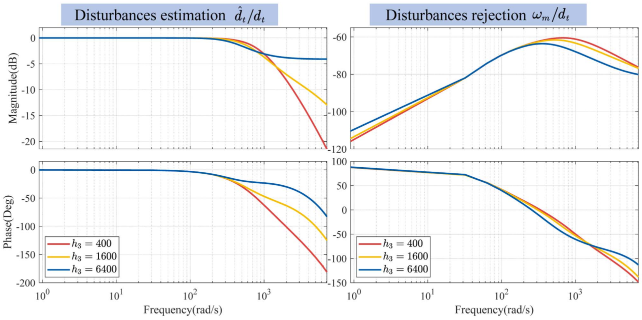

Fig. 7. Bode diagrams of PLESO under different values of h_3.

the PLESO significantly improves disturbance rejection across the frequency spectrum.

To evaluate the effect of parameter tuning on PLESO performance, we conduct a series of frequency-sweep analyses in which the key parameters, i.e., α and h_3, are systematically varied. Specifically, α is set to 0.75, 0.9, and 0.975, while h_3 is varied as 400, 1600, and 6400. The resulting frequency responses for disturbance estimation performance $\hat{d}_t/d_t$ and disturbance rejection performance ω_m/d_t are shown in Figs. 6 and 7, respectively.

As illustrated in Fig. 6, decreasing α enhances disturbance rejection in the low-to-medium frequency range, while increasing α improves estimation performance in the high-frequency range. However, excessively small values may induce chattering, whereas overly large values degrade disturbance rejection performance.

As shown in Fig. 7, increasing h_3 amplifies the effect of the differential term, thereby enhancing disturbance estimation performance, particularly in the high-frequency range. However, this improvement may slightly degrade disturbance rejection capability in the low-frequency range, revealing a tradeoff between estimation accuracy and robustness.

Remark 3: The gain h_3 in (15) is tuned to meet the desired observer performance. As illustrated by the Bode plots in Fig. 7, we evaluated $h_3 \in \{400, 1600, 6400\}$. Increasing h_3 amplifies the differential term and thereby improves the estimation of high-frequency disturbances. However, a larger h_3 slightly degrades low-frequency disturbance rejection, indicating a tradeoff between estimation accuracy and robustness. Considering this tradeoff, we select $h_3 = 1600$ as a balanced setting that yields favorable overall control performance.

To establish the finite-time convergence property of the PLESO, the following theorem is presented. Note that the finite-time convergence refers to the case where the convergence time of the disturbance estimation error is bounded within a finite interval.

Theorem 1: Under Assumption 1, there exists a positive constant a_1 such that the estimation errors of the PLESO defined by (15), i.e., $e_1 = \omega_m - \hat{\omega}_m$ and $e_2 = d_t - \hat{d}_t$, converge in finite time to the following region:

$$\begin{aligned} R = \Bigg\{ (e_1, e_2) : |e_1| &\le g_2^{\frac{1}{1+\alpha}} \left(\frac{2}{\alpha}\right)^{\frac{1}{2}} \left(\frac{g_1 D_{\max}}{a_1(1-\varepsilon)}\right)^{\frac{2}{\beta}} \\ &\quad + \sqrt{2}\, g_2^{\frac{1}{1+\alpha}} \left(\frac{g_1 D_{\max}}{a_1(1-\varepsilon)}\right)^{\frac{1}{\beta}} \\ |e_2| &\le a_1 g_2^{\frac{\alpha}{\beta}} \left(\frac{2}{\alpha}\right)^{\frac{\alpha}{2}} \left(\frac{g_1 D_{\max}}{a_1(1-\varepsilon)}\right)^{\frac{\alpha}{\beta}} \Bigg\} \end{aligned} \tag{17}$$

where g_1 and g_2 are positive constants. Furthermore, $\varepsilon \in (0, 1)$ is an arbitrarily small constant.

Proof: Define $\sigma_1 = e_1$ and $\sigma_2 = e_2/h_1$, where $e_2 = d_t - \hat{d}_t$. Then, the evolution of σ_1 and σ_2 is described by

$$\begin{cases} \dot{\sigma}_1 = a_1 p_1 \\ \dot{\sigma}_2 = -a_2(p_2 + p_3) + \dfrac{\eta}{a_1} \end{cases} \tag{18}$$

with $a_1 = h_1$, $a_2 = h_2/h_1$, and $\eta = \dot{d}_t - h_3 \dot{e}_{1c}$. The auxiliary functions are defined as follows:

$$\begin{aligned} &p_1 = -\lfloor \sigma_1 \rceil^{\alpha} + \sigma_2, p_2 = -\lfloor \sigma_2 \rceil^{\frac{\beta}{\alpha}} \\ &p_3 = -\lfloor \sigma_1 \rceil^{\beta} + \lfloor \sigma_2 \rceil^{\frac{\beta}{\alpha}}, p_4 = -\sigma_1 + \lfloor \sigma_2 \rceil^{\frac{1}{\alpha}}. \end{aligned} \tag{19}$$

Then, we apply the technique of adding a power integrator to formulate a homogeneous Lyapunov function

$$V(\sigma_1, \sigma_2) = E_1(\sigma_1, \sigma_2) + E_2(\sigma_2) \tag{20}$$

with $E_1(\sigma_1, \sigma_2) = \frac{1}{2}(\sigma_1 - \lfloor \sigma_2 \rceil^{\frac{1}{\alpha}})^2$, $E_2(\sigma_2) = \frac{\alpha}{2}|\sigma_2|^{\frac{2}{\alpha}}$. The time derivative of the Lyapunov function (20) is given by $\dot{V}(\sigma_1, \sigma_2) = \dot{E}_1(\sigma_1, \sigma_2) + \dot{E}_2(\sigma_2)$.

Since $0 < \frac{\beta}{\alpha} < 1$, it follows from Lemma 2 [54] that:

$$|p_3| \le 2^{\frac{1-\alpha}{\alpha}} |p_1|^{\frac{\beta}{\alpha}}. \tag{21}$$

Selecting $a_2 \ge 2$, and considering the fact that $\partial E_2(\sigma_2)/\partial \sigma_2 = -\lfloor p_2 \rceil^{\frac{2-\alpha}{\beta}}$, it follows that:

$$\begin{aligned} \dot{E}_2(\sigma_2) &= \frac{\partial E_2(\sigma_2)}{\partial \sigma_2} \cdot \dot{\sigma}_2 \\ &\le -2\,|p_2|^{\frac{1+\alpha}{\beta}} - a_2 \lfloor p_2 \rceil^{\frac{2-\alpha}{\beta}} p_3 + \frac{\partial E_2(\sigma_2)}{\partial \sigma_2} \cdot \frac{\eta}{a_1}. \end{aligned} \tag{22}$$

By using (21) and Lemma 3, we obtain

$$a_2 \left| \lfloor p_2 \rceil^{\frac{2-\alpha}{\beta}} p_3 \right| \le \frac{1}{2}|p_2|^{\frac{1+\alpha}{\beta}} + \gamma_1 |p_1|^{\frac{1+\alpha}{\alpha}} \tag{23}$$

where γ_1 is a positive constant.

By substituting (23) into (22), one obtains

$$\dot{E}_2(\sigma_2) \leq -\frac{3}{2}|p_2|^{\frac{1+\alpha}{\beta}} + \gamma_1 |p_1|^{\frac{1+\alpha}{\alpha}} + \frac{\partial E_2(\sigma_2)}{\partial \sigma_2} \cdot \frac{\eta}{a_1}. \tag{24}$$

Similarly, the term $\dot{E}_1(\sigma_1, \sigma_2)$ can be expressed as

$$\begin{aligned}\dot{E}_1(\sigma_1, \sigma_2) = \frac{1}{\alpha}\, |p_2|^{\frac{1-\alpha}{\beta}}\, a_2(p_2 + p_3)p_4 + (\sigma_1 - \lfloor \sigma_2 \rceil^{\frac{1}{\alpha}})a_1 p_1 \\ + \frac{\partial E_1(\sigma_1, \sigma_2)}{\partial \sigma_2} \cdot \frac{\eta}{a_1}.\end{aligned} \tag{25}$$

By employing Lemma 1, we have

$$\begin{aligned}|p_4| &= \left| \lfloor \sigma_2 \rceil^{\frac{1}{\alpha}} - \sigma_1 \right| \\ &\leq l \left(|p_1|^{\frac{1}{\alpha}} + |p_1| \cdot |\sigma_2|^{\frac{1-\alpha}{\alpha}} \right)\end{aligned} \tag{26}$$

where $l = \frac{1}{\alpha}(2^{\frac{-\beta}{\alpha}} + 2)$. Furthermore, a direct computation yields

$$|p_4| \leq l|p_1|^{\frac{1}{\alpha}} + l|p_1| \cdot |p_2|^{\frac{1-\alpha}{\alpha}}. \tag{27}$$

From Lemma 3, we have

$$\frac{1}{\alpha}\, |p_2|^{\frac{1-\alpha}{\beta}}\, a_2 p_2 p_4 \leq \frac{1}{4}|p_2|^{\frac{1+\alpha}{\beta}} + \gamma_2 |p_1|^{\frac{1+\alpha}{\alpha}} \tag{28}$$

where γ_2 is a positive constant.

Similarly, one arrives at

$$\frac{1}{\alpha}|p_2|^{\frac{1-\alpha}{\beta}} a_2 p_3 p_4 \leq \frac{1}{4}|p_2|^{\frac{1+\alpha}{\beta}} + \gamma_3 |p_1|^{\frac{1+\alpha}{\alpha}} \tag{29}$$

where γ_3 is a positive constant.

Moreover, leveraging the fact $\frac{1}{\alpha} > 1$ and applying Lemma 1, it is evident that

$$\begin{aligned}&\left(\sigma_1 - \lfloor \sigma_2 \rceil^{\frac{1}{\alpha}}\right) a_1 p_1 \\ &\leq -a_1 2^{\frac{\alpha-1}{\alpha}}\, \left|\sigma_2 - \lfloor \sigma_1 \rceil^{\alpha}\right|^{\frac{1+\alpha}{\alpha}} \\ &= -a_1 2^{\frac{\alpha-1}{\alpha}}\, |p_1|^{\frac{1+\alpha}{\alpha}}.\end{aligned} \tag{30}$$

Substituting (28), (29), and (30) into (25) yields

$$\begin{aligned}\dot{E}_1(\sigma_1, \sigma_2) \leq \frac{1}{2}\, |p_2|^{\frac{1+\alpha}{\beta}} + \left(\gamma_2 + \gamma_3 - a_1 2^{\frac{\alpha-1}{\alpha}}\right) |p_1|^{\frac{1+\alpha}{\alpha}} \\ + \frac{\partial E_1(\sigma_1, \sigma_2)}{\partial \sigma_2} \cdot \frac{\eta}{a_1}.\end{aligned} \tag{31}$$

Combining (24) and (31), $\dot{V}(\sigma_1, \sigma_2)$ satisfies

$$\begin{aligned}\dot{V}(\sigma_1, \sigma_2) \leq\; -|\sigma_2|^{\frac{1+\alpha}{\alpha}} + \left(\gamma_1 + \gamma_2 + \gamma_3 - a_1 2^{\frac{\alpha-1}{\alpha}}\right) |p_1|^{\frac{1+\alpha}{\alpha}} \\ + \frac{\partial V(\sigma_1, \sigma_2)}{\partial \sigma_2} \cdot \frac{\eta}{a_1}.\end{aligned} \tag{32}$$

Furthermore, the constant a_1 can be selected as

$$a_1 \geq 2^{\frac{1-\alpha}{\alpha}} \left(\gamma_1 + \gamma_2 + \gamma_3 + 1\right). \tag{33}$$

Substituting (33) into (32) yields

$$\dot{V}(\sigma_1, \sigma_2) \leq -H(\sigma_1, \sigma_2) + \frac{\partial V(\sigma_1, \sigma_2)}{\partial \sigma_2} \cdot \frac{\eta}{a_1} \tag{34}$$

where $H(\sigma_1, \sigma_2) = |p_1|^{\frac{1+\alpha}{\alpha}} + |p_2|^{\frac{1+\alpha}{\beta}}$.

Thus, according to Assumption 1, we have

$$\dot{V}(\sigma_1, \sigma_2) \leq -H(\sigma_1, \sigma_2) + \left| \frac{\partial V(\sigma_1, \sigma_2)}{\partial \sigma_2} \right| \cdot \frac{D_{\max}}{a_1}. \tag{35}$$

With the upper bound of the Lyapunov function derivative established; we now proceed to prove the finite-time convergence of the PLESO. Define the region Q_1 as $\left\{(\sigma_1, \sigma_2) : |p_1|^{\frac{1+\alpha}{\alpha}} + |p_2|^{\frac{1+\alpha}{\beta}} \leq (\frac{g_1 D_{\max}}{a_1(1-\epsilon)})^{\frac{1+\alpha}{\beta}} \right\}$, where $g_1 > 0$ and $0 < \epsilon < 1$. Based on (35), $\dot{V}(\sigma_1, \sigma_2) < 0$ for $(\sigma_1, \sigma_2) \notin Q_1$. Notably, both $|\frac{\partial V(\sigma_1, \sigma_2)}{\partial \sigma_2}|$ and $H^{\frac{2-\alpha}{1+\alpha}}$ share the same homogeneity degree of $2 - \alpha$ under the scaling weight $(1, \alpha)$. Therefore, by Lemma 4, $|\frac{\partial V(\sigma_1, \sigma_2)}{\partial \sigma_2}| \leq g_1 \cdot H^{\frac{2-\alpha}{1+\alpha}}(\sigma_1, \sigma_2)$ holds. Consequently, (35) can be expressed as

$$\dot{V}\left(\sigma_1, \sigma_2\right) \leq -H\left(\sigma_1, \sigma_2\right) + \frac{g_1 D_{\max}}{a_1} \cdot H^{\frac{2-\alpha}{1+\alpha}}\left(\sigma_1, \sigma_2\right). \tag{36}$$

When $(\sigma_1, \sigma_2) \notin Q_1$, (36) simplifies to

$$\dot{V}(\sigma_1, \sigma_2) < -\epsilon H(\sigma_1, \sigma_2) < 0. \tag{37}$$

Define another region Q_2 as $\left\{(\sigma_1, \sigma_2) : V(\sigma_1, \sigma_2) \leq N, N = g_2^{\frac{2}{1+\alpha}} (\frac{g_1 D_{\max}}{a_1(1-\epsilon)})^{\frac{2}{\beta}} \right\}$ where g_2 is a positive constant. Subsequently, it can be shown that $\dot{V}(\sigma_1, \sigma_2) < 0$ when $(\sigma_1, \sigma_2) \notin Q_2$, where Q_1 is a subset of Q_2.

Therefore, the set Q_2 becomes an attractive region, and there exists a finite positive constant T_0 such that for all $T > T_0$, the trajectory (σ_1, σ_2) enters and remains within Q_2. In other words, for $T > T_0$, we have $V(\sigma_1, \sigma_2) \leq N$.

For $T \geq T_0$, it follows from the definition of the Lyapunov function that:

$$E_2(\sigma_2) = \frac{\alpha}{2}|\sigma_2|^{\frac{2}{\alpha}} \leq V(\sigma_1, \sigma_2) \leq N. \tag{38}$$

Given $a_1 = h_1$ and $\sigma_2 = e_2/h_1$, the results in (38) leads to

$$|e_2| \leq a_1 g_2^{\frac{\alpha}{\beta}} \left(\frac{2}{\alpha}\right)^{\frac{\alpha}{2}} \left(\frac{g_1 D_{\max}}{a_1(1-\varepsilon)}\right)^{\frac{\alpha}{\beta}}. \tag{39}$$

Next, we estimate the convergence domain of e_1. For all $T \geq T_0$, we have

$$E_1(\sigma_1, \sigma_2) = \frac{1}{2}(\sigma_1 - \lfloor \sigma_2 \rceil^{\frac{1}{\alpha}})^2 \leq V(\sigma_1, \sigma_2) \leq N. \tag{40}$$

Then, we obtain the following result:

$$\left|\sigma_1 - \lfloor \sigma_2 \rceil^{\frac{1}{\alpha}}\right| \leq \sqrt{2}\, g_2^{\frac{1}{1+\alpha}} \left(\frac{g_1 D_{\max}}{a_1(1-\varepsilon)}\right)^{\frac{1}{\beta}}. \tag{41}$$

From (39), we further have

$$\begin{aligned}&|e_1| \leq |\lfloor \sigma_2 \rceil^{\frac{1}{\alpha}}| + \left|\sigma_1 - \lfloor \sigma_2 \rceil^{\frac{1}{\alpha}}\right| \\ &\leq g_2^{\frac{1}{1+\alpha}} \left(\frac{2}{\alpha}\right)^{\frac{1}{2}} \left(\frac{g_1 D_{\max}}{a_1(1-\varepsilon)}\right)^{\frac{2}{\beta}} + \sqrt{2}\, g_2^{\frac{1}{1+\alpha}} \left(\frac{g_1 D_{\max}}{a_1(1-\varepsilon)}\right)^{\frac{1}{\beta}}.\end{aligned} \tag{42}$$

This implies that the estimation errors of the PLESO defined by (15), i.e., $e_1 = \omega_m - \hat{\omega}_m$ and $e_2 = d_t - \hat{d}_t$, converge to the region R in finite time T_0. Therefore, the proof is complete.

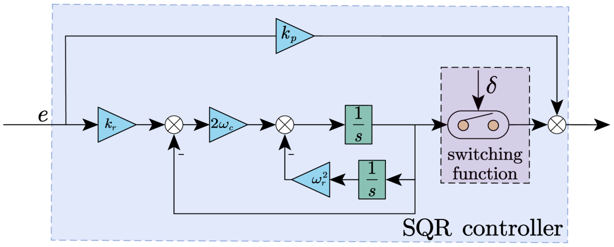

Fig. 8. SQR controller.

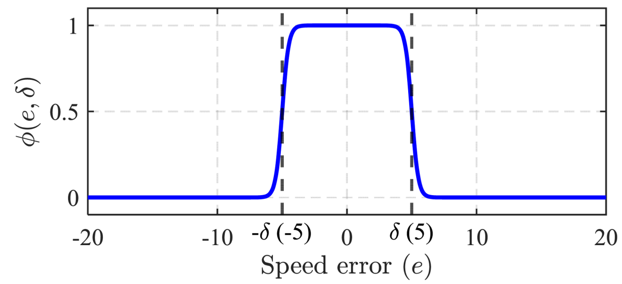

Fig. 9. Switching function when $\delta = 5$ rpm and $k = 4$.

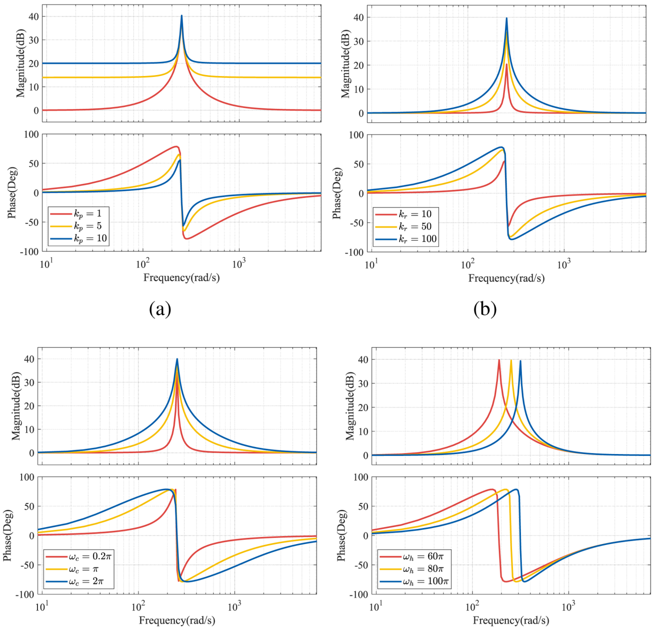

(a) (b)

(c) (d)

Fig. 10. Bode diagrams of the SQR controller with different parameters. (a) k_p. (b) k_r. (c) ω_c. (d) ω_h.

B. Design of the SQR-Based Feedback Control

Although the PLESO enhances disturbance estimation performance within its bandwidth, its capability to suppress periodic disturbances remains limited. Increasing the observer bandwidth can improve estimation accuracy but also leads to greater sensitivity to measurement noise, potentially compromising overall PMSM performance.

Therefore, to effectively suppress persistent periodic disturbances, it is beneficial to incorporate an additional periodic disturbance rejection mechanism into the control loop. A widely adopted solution is the QR controller [55], formulated as follows:

$$G_{\text{QR}}(s) = k_p + \frac{2k_r\omega_c s}{s^2 + 2\omega_c s + {\omega_h}^2} \tag{43}$$

where ω_h is the resonant frequency, ω_c is the cutoff frequency and k_r is the resonant gain.

Nevertheless, the QR controller introduces fixed resonant terms, which may adversely affect the dynamic response of the PMSM system. To mitigate this issue, we propose an SQR controller that employs a switching resonant term. As shown in Fig. 8, the SQR controller modulates the resonant action based on the speed error magnitude, allowing the resonant term to take effect only when necessary.

To this end, the fundamental SQR controller is designed as

$$G_{\text{SQR}}(s) = k_p + \frac{2k_r\omega_c s}{s^2 + 2\omega_c s + \omega_h^2} \cdot \phi(e, \delta) \tag{44}$$

where $\phi(e, \delta) \in [0, 1]$ is a smooth switching function that determines the activation degree of the resonant path.

Specifically, the switching function $\phi(e, \delta)$ is defined as

$$\phi(e, \delta) = 1 - \frac{1}{1 + \exp(-k(|e| - \delta))} \tag{45}$$

where $e = \omega_{\text{ref}} - \omega_m$ denotes the speed error, δ is the switching threshold, and $k > 0$ determines the steepness of the transition. The switching function enables a smooth transition of the resonant effect as the speed error crosses the threshold.

Fig. 9 illustrates the shape of $\phi(e, \delta)$ for $\delta = 5$ rpm and $k = 4$, showing its smooth and continuous switching behavior from 0 to 1.

Remark 4: For the switching function in (45), δ defines the activation threshold, whereas k determines the speed and smoothness of switching. Together, these parameters enable the SQR controller to selectively attenuate small periodic speed fluctuations during steady-state operation. Specifically, δ sets the activation band and sensitivity: a larger δ widens the operating band, whereas a smaller δ confines activation to minor periodic disturbances. In practice, a moderate choice (e.g., $\delta = 5$ rpm) offers a favorable tradeoff between ripple suppression and transient stability. In addition, k governs the activation dynamics of the SQR controller. A larger k accelerates switching, enabling rapid compensation of periodic fluctuations but potentially reducing the stability margin, whereas a smaller k smooths transitions and mitigates chattering. In hardware implementation, setting $k = 4$ yields smooth yet effective switching behavior.

To evaluate the frequency-domain behavior of the proposed SQR controller and gain insight into the effect of its key parameters, Bode diagrams under various configurations are presented in Fig. 10. First, with $k_r = 100$, $\omega_c = \pi$ rad/s, and $\omega_h = 80\pi$ rad/s, the influence of the proportional gain k_p is examined for $k_p = 1, 5, 10$, as shown in Fig. 10(a). Increasing k_p enhances the overall disturbance rejection capability of the PMSM control system. Next, with $k_p = 1$, $\omega_c = \pi$ rad/s, and

$\omega_h = 80\pi$ rad/s, the Bode diagrams for $k_r = 10, 50, 100$ are illustrated in Fig. 10(b). A larger k_r improves the harmonic suppression at the target resonant frequency ω_h. Subsequently, with $k_p = 1$, $k_r = 100$, and $\omega_h = 80\pi$ rad/s, the impact of ω_c is analyzed for $\omega_c = 0.2\pi$ rad/s, π rad/s, 2π rad/s, as shown in Fig. 10(c). Adjusting ω_c modifies the control bandwidth while preserving its attenuation effect at ω_h. Finally, with $k_p = 1, k_r = 100$, and $\omega_c = \pi$ rad/s, the Bode diagrams for $\omega_h = 60\pi$ rad/s, 80π rad/s, 100π rad/s are shown in Fig. 10(d). From these results, we can see that the SQR controller consistently exhibits high gain at the resonant frequency ω_h, enabling effective suppression of harmonic components.

Building upon the design in (44) and the switching mechanism defined in (45), multiple SQR controllers can be embedded in the feedback control law to address the dominant periodic disturbances. According to the analysis in Section II-A, the dominant components are the first- and second-order speed harmonics. Therefore, the SQR-based feedback controller is designed as

$$G'_{\mathrm{SQR}}(s) = k_p + \left(\frac{2k_{r1}\omega_{c1}s}{s^2 + 2\omega_{c1}s + \omega_{h1}^2} + \frac{2k_{r2}\omega_{c2}s}{s^2 + 2\omega_{c2}s + \omega_{h2}^2}\right) \times \phi(e, \delta) \tag{46}$$

where $\omega_{h1} = \omega_e$ and $\omega_{h2} = 2\omega_e$.

By integrating the PLESO-based feedforward controller with the SQR-based feedback controller, the composite speed control scheme for the PMSM is designed as

$$i_q^* = i_{qb} + i_{qf} \tag{47}$$

where $i_{qb} = \mathcal{L}^{-1}(G'_{\mathrm{SQR}}(s)E(s))$ is the output of the SQR controller, $\mathcal{L}^{-1}$ denotes the inverse Laplace transform, and $E(s)$ is the Laplace transform of the speed error $e(t)$.

Remark 5: As noted in [56], resonant terms can degrade the dynamic performance of PMSM speed control. To mitigate this, the switching mechanism in the SQR controller is applied after the QR block. In this configuration, only the QR terms are activated during switching, which prevents the adverse impact on the overall control loop. This arrangement ensures consistent disturbance rejection performance under both transient and steady-state conditions.

Remark 6: The proposed control scheme consists of two independent components: the PLESO-based feedforward controller and the SQR-based feedback controller. As shown in Fig. 2, the parameters of each component can be tuned separately. This is because the SQR-based feedback controller operates in parallel with the PLESO and is primarily responsible for compensating periodic disturbances that the PLESO alone cannot fully suppress.

IV. EXPERIMENTAL RESULTS AND DISCUSSION

To validate the performance of the proposed control scheme, comparative experiments are conducted on a 1.5 kW three-phase PMSM platform, as shown in Fig. 11. The platform is equipped with a three-phase PMSM 130ST-M10015 and an RTU-BOX204 real-time digital controller. The key parameters of the PMSM are listed in Table I.

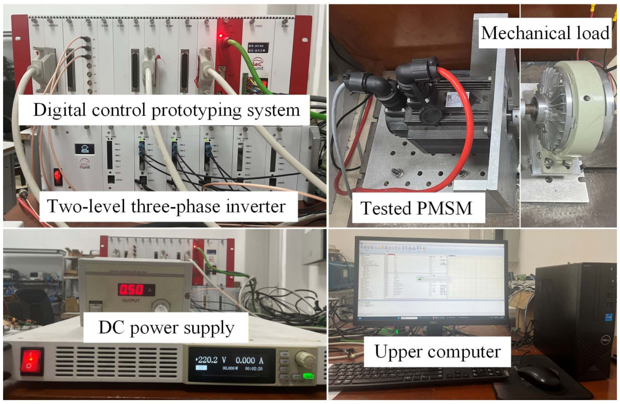

Fig. 11. Experimental platform of the PMSM drive system.

TABLE I
KEY PARAMETERS OF THE PMSM PLATFORM

Parameter	Unit	Value
Rated speed S_r	rpm	1500
Rated phase current I_r	A	6
Stator inductance L_s	mH	4.37
Number of poles p_n	–	44
Rated power P_r	kW	1.5
Flux linkage ψ_f	wb	0.142
Rated torque T_r	N/m	10
Stator resistance R_s	Ω	1.5
Moment of inertia J	kg/m^2	0.00194

Subsequently, a series of comparative experiments will be conducted to assess the suppression performance of the proposed control scheme against both periodic and aperiodic disturbances. In all experiments, the current loop is regulated by a PI controller with proportional and integral gains set to $k_p^i = 2$ and $k_i^i = 20$, respectively.

A. Speed Tracking Performance

First, the speed tracking performance of the PMSM system under different observers is evaluated by applying a sinusoidal reference signal $\omega_{\mathrm{ref}} = 400 + 200\sin(\pi t)$. Here, four observer-based proportional controllers, namely the LESO-based [57], SESO-based, MSESO-based, and PLESO-based proportional controllers, are implemented under identical conditions. The speed control loop adopts a proportional controller with the gain $k_p = 10$.

For fair comparison, the bandwidths of the four observers are uniformly set to $\omega_0 = 200\,\mathrm{rad/s}$. The SESO and MSESO employ the same gains as the LESO, with an additional setting of $\alpha = 0.75$. The PLESO uses the same h_1, h_2, and α as the MSESO, along with an additional gain $h_3 = h_1 = 400$. The resulting speed responses are illustrated in Fig. 12. Meanwhile, the comparative performance indices are summarized in Table II.

As detailed in Table II, among the four observer-based proportional controllers, the PLESO-based controller yields the

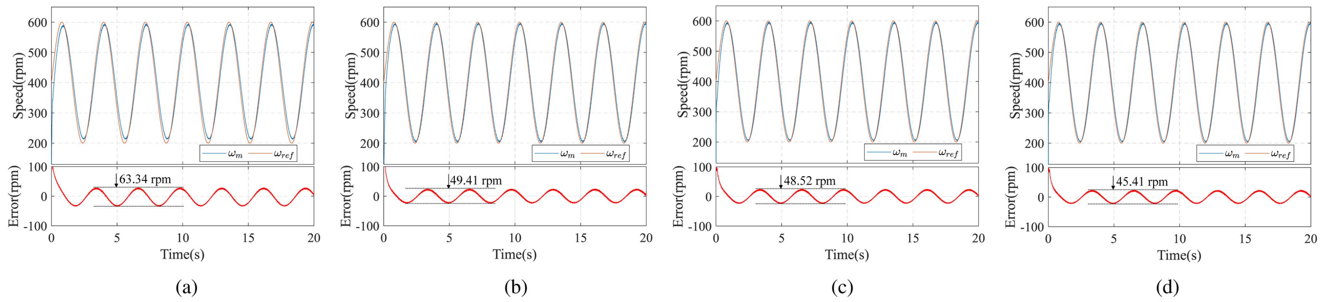

Fig. 12. Comparison of sinusoidal speed responses under four ESOs with the same proportional controller. (a) LESO. (b) SESO. (c) MSESO. (d) PLESO.

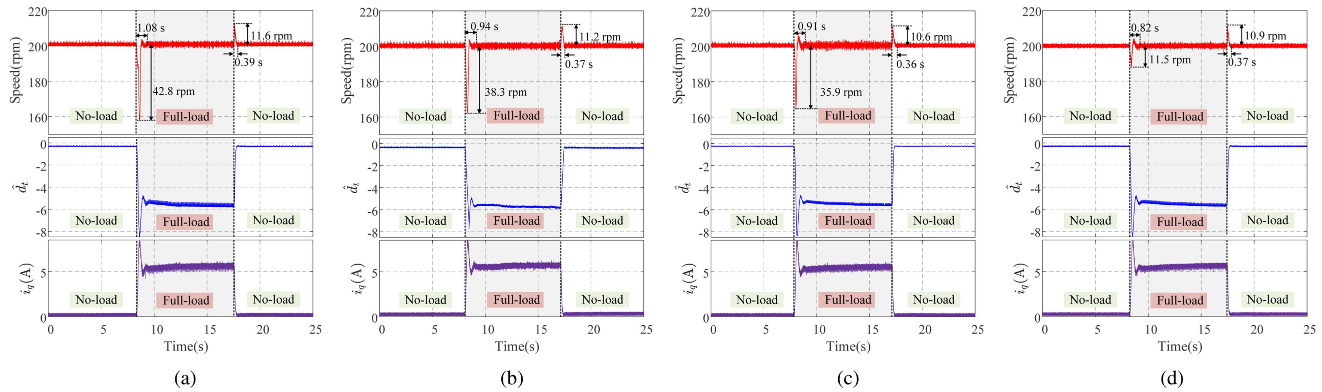

Fig. 13. Comparison of disturbance rejection performance under four ESOs with the same proportional controller. (a) LESO. (b) SESO. (c) MSESO. (d) PLESO.

TABLE II
SPEED TRACKING PERFORMANCE UNDER SINUSOIDAL REFERENCE

Observer	Tracking error magnitude (rpm)
LESO	63.34
SESO	49.41
MSESO	48.52
PLESO	45.41

TABLE III
APERIODIC DISTURBANCE REJECTION PERFORMANCE

Observer	Speed drop (rpm)	Settling time (s)
LESO	42.8	1.08
SESO	38.3	0.94
MSESO	35.9	0.91
PLESO	11.5	0.82

smallest error amplitude of 45.41 rpm, followed by the MSESO-based controller (48.52 rpm), the SESO-based controller (49.41 rpm), and the LESO-based controller (63.34 rpm). These results indicate that the PLESO-based controller achieves the best steady-state tracking performance. This improvement is primarily attributed to the enhanced capability of the PLESO in accurately and rapidly estimating total disturbances under time-varying reference signals.

B. Aperiodic Disturbance Rejection Performance

Next, to validate the aperiodic disturbance rejection capability, experimental results under a step change in load torque are presented in Fig. 13, comparing four observers: the LESO, SESO, MSESO, and PLESO. All controllers are implemented in the speed control loop using the proportional controller with the gain $k_p = 10$. Four observer configurations are tested: LESO, SESO, MSESO, and PLESO, with all observer parameters kept identical to those in Section IV-A.

The comparative performance indices are summarized in Table III. As shown in Fig. 13(a) and Table III, under the LESO-based proportional controller, during a step load increase, the speed drops by 42.8 rpm with a settling time of 1.08 s. When the load is removed, the speed overshoot reaches 11.6 rpm, with a settling time of 0.39 s. Under the SESO-based proportional controller [see Fig. 13(b)], the speed drop during load application is 38.3 rpm, with a settling time of 0.94 s, and the speed overshoot during load removal is 11.2 rpm, with a settling time of 0.37 s. With the MSESO-based proportional controller [see Fig. 13(c)], the speed drop reduces to 35.9 rpm and the settling time shortens to 0.91 s; the speed overshoot during load drop is 10.6 rpm, with a settling time of 0.36 s. Finally, under the PLESO-based proportional controller [see Fig. 13(d)], the speed drop is further reduced to 11.5 rpm with a settling time of 0.82 s,

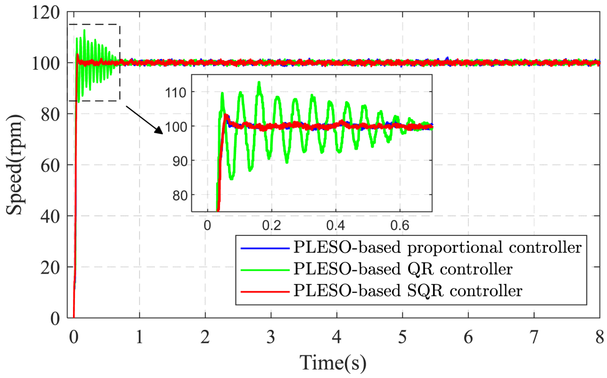

Fig. 14. Speed responses of PLESO-based controllers: proportional, QR, and SQR at 100 rpm.

and the speed overshoot during load removal is 10.9 rpm, with a settling time of 0.37 s.

Based on the above-mentioned results, we can draw the conclusion that the PLESO-based feedforward controller demonstrates better aperiodic disturbance rejection performance compared to the LESO-based, SESO-based, and MSESO-based feedforward controllers.

C. Periodic Disturbance Suppression Performance

Subsequently, comparative experiments are conducted to evaluate the effectiveness of the proposed SQR-based feedback controller in suppressing periodic disturbances. Three configurations are tested: the PLESO-based proportional controller, the PLESO-based QR controller, and the PLESO-based SQR controller. According to the analysis in [6], the speed control loop is primarily affected by low-frequency and interharmonic periodic disturbances. Therefore, the reference speed is set to 100 rpm.

In all configurations, the observer parameters of the PLESO are kept identical to those in Section IV-A. The proportional controller adopts a gain of $k_p = 10$. For the QR controller, the parameters are configured as follows $k_p = 10$, $\omega_{h1} = \omega_e$, $\omega_{h2} = 2\omega_e$, and $\omega_{ci} = 1.5\%\omega_{hi}\ (i = 1, 2)$, with resonant gains $k_{r1} = 10$ and $k_{r2} = 2k_{r1}$. The SQR controller shares the same values of ω_{hi}, ω_{ci}, and $k_i\ (i = 1, 2)$ as the QR controller, with an additional $\delta = 5$.

Fig. 14 compares the speed responses of the three controllers at a reference speed of $\omega_{\text{ref}} = 100$ rpm. It is evident that the introduction of the PLESO-based QR controller significantly degrades the dynamic performance of the PMSM system, leading to a prolonged settling time due to speed fluctuations induced by the resonant terms. In contrast, the speed response of the PLESO-based SQR controller closely resembles that of the PLESO-based proportional controller, exhibiting only minor fluctuations that rapidly decay after reaching steady state. Thus, compared with the PLESO-based QR controller, the PLESO-based SQR controller mitigates adverse effects and enables faster disturbance rejection capability.

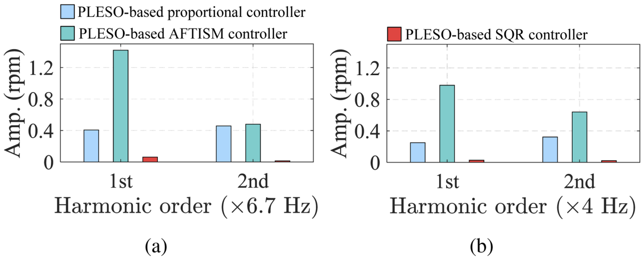

(a) (b)

Fig. 15. Harmonic suppression at different speeds. (a) 100 rpm. (b) 60 rpm.

TABLE IV
PERIODIC DISTURBANCE SUPPRESSION PERFORMANCE

Speed (rpm)	Controller	Ripple (rpm)	First harm.	Second harm.
100	PLESO-based proportional	3.82	0.406	0.458
	PLESO-based AFTISM	3.58	1.42	0.48
	PLESO-based SQR	2.08	0.062	0.014
60	PLESO-based proportional	3.28	0.25	0.322
	PLESO-based AFTISM	3.12	0.98	0.64
	PLESO-based SQR	1.73	0.028	0.022

To further assess the periodic disturbance suppression capability of the PLESO-based SQR controller, we introduce an additional benchmark controller, namely the adaptive fixed-time integral sliding-mode (AFTISM) controller proposed in [58], to serve as a basis for comparison. Here, additional comparative experiments are conducted using three control configurations: the PLESO-based proportional controller, the PLESO-based AFTISM controller, and the PLESO-based SQR controller.

The AFTISM controller features a fixed-time integral sliding surface and an adaptive reaching law. Following [58], the integral sliding surface and its reaching law are developed as

$$s(t) = e(t) - e(0) + \int_0^t \left(\alpha_1 \lfloor e \rceil^{k_1} + \beta_1 \lfloor e \rceil^{k_2}\right) d\mu \tag{48}$$

$$\dot{s} = -\alpha_2 \lfloor s \rceil^{k_3} - \beta_2 \lfloor s \rceil^{k_4} - \hat{k}\,\text{sign}(s) \tag{49}$$

where $k_1 = m_1^{\text{sign}(|s|-1)}$, $k_2 = m_2^{\text{sign}(1-|s|)}$, $k_3 = m_3^{\text{sign}(|s|-1)}$, $k_4 = m_4^{\text{sign}(1-|s|)}$, $\alpha_1,\ \beta_1,\ \alpha_2,\ \beta_2 > 0$, $m_3 > 1$, $0 < m_4 < 1$, and the adaptive gain is

$$\hat{k} = l|e|\frac{1 + \lambda - e^{-\eta|s|}}{\lambda}, \quad 0 < \lambda < 1,\ l > 0,\ \eta > 0. \tag{50}$$

The corresponding current reference is computed as

$$\begin{aligned} i_q^* = \frac{1}{K}\Big(&\dot{\omega}_{ref} + \alpha_1 \lfloor e \rceil^{k_1} + \beta_1 \lfloor e \rceil^{k_2} + \alpha_2 \lfloor s \rceil^{k_3} \\ &+ \beta_2 \lfloor s \rceil^{k_4} + \hat{k}\,\text{sign}(s)\Big). \end{aligned} \tag{51}$$

The speed ripple and harmonic amplitudes for the proposed approach and state-of-the-art methods are listed in Table IV.

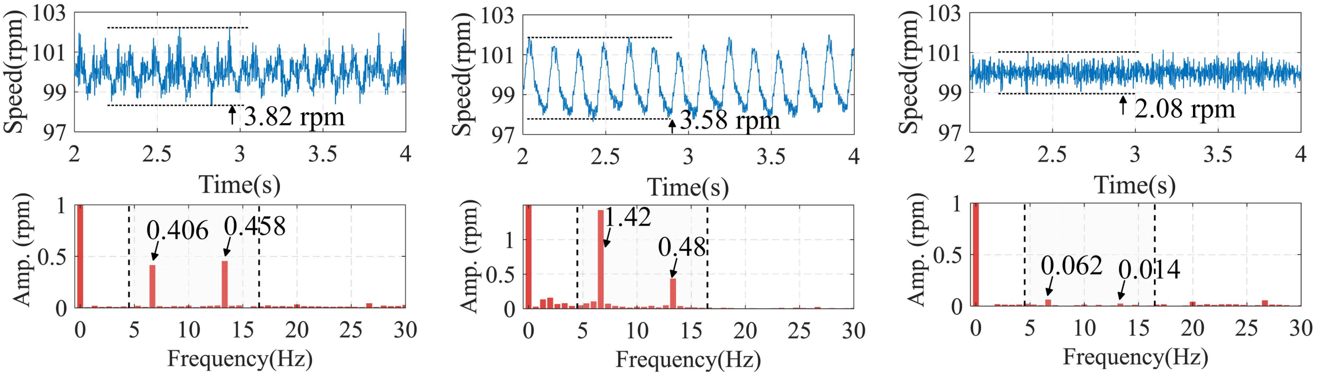

(a) (b) (c)

Fig. 16. Harmonic suppression performance at 100 rpm. (a) PLESO-based proportional controller. (b) PLESO-based AFTISM controller. (c) PLESO-based SQR controller.

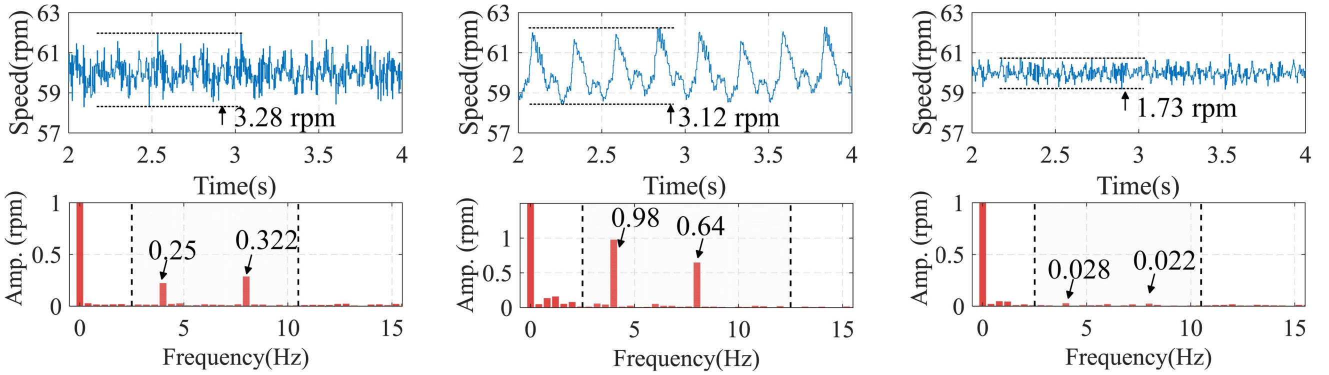

(a) (b) (c)

Fig. 17. Harmonic suppression performance at 60 rpm. (a) PLESO-based proportional controller. (b) PLESO-based AFTISM controller. (c) PLESO-based SQR controller.

Fig. 16(a)–(c) shows the speed responses and FFT spectra at 100 rpm. The PLESO-based proportional controller yields a steady-state speed fluctuation of 3.82 rpm, with first- and second-harmonic amplitudes of 0.406 and 0.458, respectively. The PLESO-based SQR controller reduces these values to 2.08 rpm, 0.062, and 0.014, respectively. Meanwhile, the PLESO-based AFTISM controller exhibits a fluctuation of 3.58 rpm, with harmonic amplitudes of 1.42 and 0.48.

Similarly, at 60 rpm, Fig. 17(a)–(c) presents the steady-state speed and FFT results. The PLESO-based proportional controller shows a speed fluctuation of 3.28 rpm, with harmonic amplitudes of 0.25 and 0.322. The PLESO-based SQR controller reduces these to 1.73 rpm, 0.028, and 0.022, while the PLESO-based AFTISM controller results in 3.12 rpm, with harmonic amplitudes of 0.98 and 0.64.

Fig. 15 summarizes the harmonic-suppression results at different speeds. It is evident that the PLESO-based SQR controller outperforms both the PLESO-based proportional and AFTISM controllers in attenuating the first and second harmonics. Although the AFTISM controller achieves fast dynamic response and strong robustness, it does not explicitly target harmonic suppression, which leads to inferior attenuation of periodic disturbances compared with the proposed PLESO-based SQR controller.

D. Speed Regulation Performance Under Inertia Mismatch

To further verify the robustness of the proposed control scheme, experimental results under variations in the PMSM parameters are presented in Fig. 18. All controller and observer parameters are kept consistent with those in Section IV-C. According to the motor model (2), the key PMSM parameter affecting the control performance is K_t, which depends on the rotor magnetic flux and rotational inertia. Therefore, to evaluate the impact of parameter variations, three sets of experiments are conducted with K_t set to its nominal value, $0.8K_t$, and $1.2K_t$, respectively.

At a reference speed of 100 rpm, each experiment consists of a no-load startup followed by a full-load condition and is conducted for all the K_t values to evaluate robustness against inertia mismatch. As shown in Fig. 18(a)–(c), the proposed PLESO-based SQR control scheme maintains satisfactory speed regulation across all conditions, demonstrating strong robustness against inertia mismatch. In general, it effectively

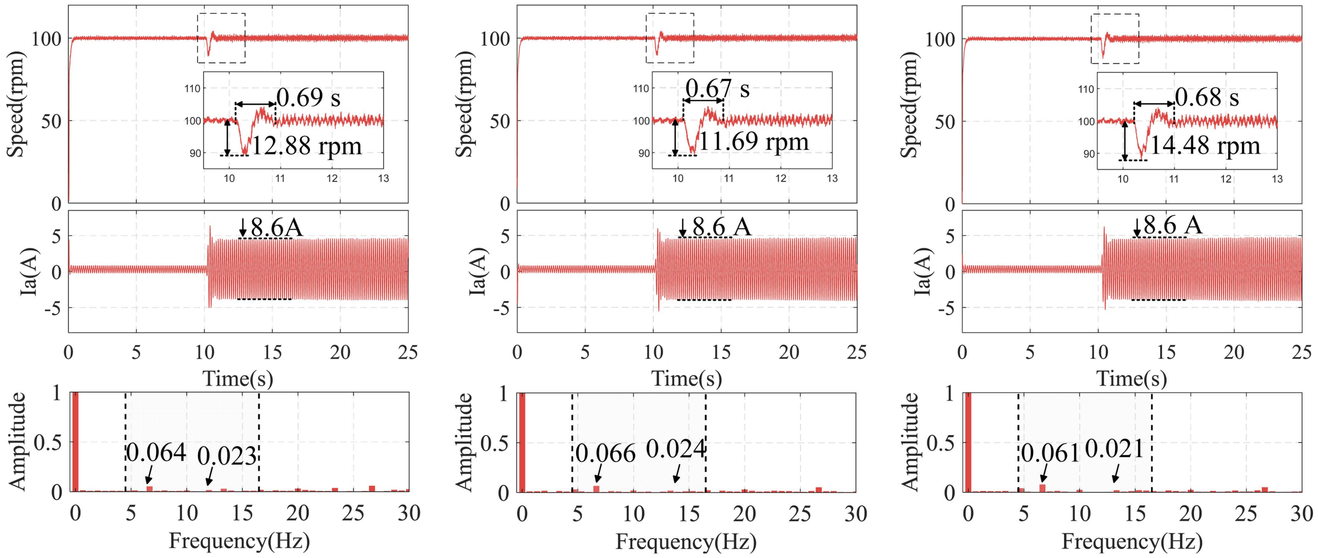

(a) (b) (c)

Fig. 18. Performance of the PLESO-based SQR controller with K_t variation. (a) K_t. (b) $0.8K_t$. (c) $1.2K_t$.

suppresses parameter variations, periodic disturbances, and aperiodic disturbances, showing clear advantages in handling various uncertainties.

V. CONCLUSION

This article investigates the speed regulation of the PMSM system subject to both periodic and aperiodic disturbances. To improve system performance, a composite control strategy is developed, featuring the PLESO-based feedforward control for aperiodic disturbance rejection and the SQR-based feedback control for periodic disturbance suppression. On the one hand, the PLESO incorporates a nonsmooth approximation to replace conventional discontinuous terms, which guarantees accurate disturbance estimation with finite-time convergence while effectively eliminating chattering effects. On the other hand, the PLESO design employs a constrained command filter to maintain bounded differential errors, thereby achieving high-performance phase-lifting observation. Furthermore, a switching mechanism is implemented in the feedback controller to minimize the negative impact of the QR controller on the PMSM system dynamics. Experimental validation demonstrates the effectiveness and robustness of the proposed control scheme in handling periodic disturbances, aperiodic disturbances, and parameter variations.

REFERENCES

[1] K. Huang et al., "An extended model predictive control for PMSM with minimum ripples and small runtimes," *IEEE Trans. Ind. Electron.*, vol. 72, no. 9, pp. 9367–9376, Sep. 2025.

[2] X. Zhang and Y. Cao, "A simple deadbeat predictive current control for PMSM with parameter robustness improvement," *IEEE J. Emerg. Sel. Topics Power Electron.*, vol. 13, no. 1, pp. 759–770, Feb. 2025.

[3] Z. Xiang, Y. Zhou, X. Zhu, L. Quan, D. Fan, and Q. Liu, "Research on characteristic airgap harmonics of a double-rotor flux-modulated PM motor based on harmonic dimensionality reduction," *IEEE Trans. Transp. Electrific.*, vol. 10, no. 3, pp. 5750–5761, Sep. 2024.

[4] J. Sun, S. Xu, S. Ding, Z. Pu, and J. Yi, "Adaptive conditional disturbance negation-based nonsmooth-integral control for PMSM drive system," *IEEE/ASME Trans. Mechatron.*, vol. 29, no. 5, pp. 3602–3613, Oct. 2024.

[5] K. Shao, J. Zheng, H. Wang, F. Xu, X. Wang, and B. Liang, "Recursive sliding mode control with adaptive disturbance observer for a linear motor positioner," *Mech. Syst. Signal Process.*, vol. 146, 2021, Art. no. 107014.

[6] S. Li, J. Yang, M. Iwasaki, and W.-H. Chen, "Hierarchical disturbance/uncertainty estimation and attenuation for integrated modeling and motion control: Overview and perspectives," *IEEE/ASME Trans. Mechatron.*, vol. 30, no. 6, pp. 4435–4449, Dec. 2025.

[7] Z. Zhou, C. Xia, Y. Yan, Z. Wang, and T. Shi, "Disturbances attenuation of permanent magnet synchronous motor drives using cascaded predictive-integral-resonant controllers," *IEEE Trans. Power Electron.*, vol. 33, no. 2, pp. 1514–1527, Feb. 2018.

[8] Y. Guo, W. Xu, J. Ge, H. Xiao, Y. Tang, and Y. Shangguan, "A DSVM-based MPC strategy with magnetizing inductance online identification method for thrust ripple suppression in linear induction machine," *IEEE Trans. Power Electron.*, vol. 40, no. 8, pp. 10746–10757, Aug. 2025.

[9] K. Mei, Q. Li, W. Chen, C.-C. Chen, and S. Ding, "Modified discrete-time super-twisting control of PMSM speed regulation system: Theory and experimentation," *IEEE Trans. Power Electron.*, vol. 40, no. 6, pp. 7980–7993, Jun. 2025.

[10] Y. Fan, J. Chen, Q. Zhang, and M. Cheng, "An improved inertia disturbance suppression method for PMSM based on disturbance observer and two-degree-of-freedom PI controller," *IEEE Trans. Power Electron.*, vol. 38, no. 3, pp. 3590–3599, Mar. 2023.

[11] J. Sun, J. Xia, S. Ding, and X. Yu, "Exact-feedback-linearization-based adaptive second-order sliding mode control design for DC–DC boost converters," *IEEE Trans. Ind. Electron.*, vol. 72, no. 5, pp. 5397–5407, May 2025.

[12] L. Guo, W. Xu, N. Jin, and H. Xiao, "A DC-offset removed sensorless control method for PMSM based on SMO with an improved prefilter and a speed immune position error compensation strategy," *IEEE Trans. Power Electron.*, vol. 40, no. 4, pp. 5163–5176, Apr. 2025.

[13] K. Shao, J. Zheng, and M. Fu, "Review on the developments of sliding function and adaptive gain in sliding mode control," *J. Autom. Intell.*, vol. 4, no. 4, pp. 266–272, 2025.

[14] S. Hou, J. Han, Y. Chu, C. Zhou, and J. Fei, "Practical terminal sliding mode control of active power filters by self-organizing hermite fuzzy neural network," *IEEE Trans. Power Electron.*, vol. 41, no. 1, pp. 626–639, Jan. 2026, doi: 10.1109/TPEL.2025.3603892.

[15] P. Chen, H. Gan, Y. Liu, and Y. Luo, "Different model-based ADRCs satisfying performance independent control for PMSM speed servo system," *IEEE Trans. Ind. Electron.*, vol. 72, no. 2, pp. 2012–2023, Feb. 2025.

[16] Z. Zhang, X. Wang, J. Xu, and Q. Zhang, "Non-cascaded robust model predictive direct speed control based on the reconstruction model and third-order ESO for SPMSM," *IEEE Trans. Power Electron.*, early access, 2025, doi: 10.1109/TPEL.2025.3639648.

[17] J. Han, "From PID to active disturbance rejection control," *IEEE Trans. Ind. Electron.*, vol. 56, no. 3, pp. 900–906, Mar. 2009.

[18] B. Guo, S. Bacha, M. Alamir, A. Hably, and C. Boudinet, "Generalized integrator-extended state observer with applications to grid-connected converters in the presence of disturbances," *IEEE Trans. Control Syst. Technol.*, vol. 29, no. 2, pp. 744–755, Mar. 2021.

[19] S. Li, J. Yang, W.-H. Chen, and X. Chen, "Generalized extended state observer based control for systems with mismatched uncertainties," *IEEE Trans. Ind. Electron.*, vol. 59, no. 12, pp. 4792–4802, Dec. 2012.

[20] S. Li and Z. Liu, "Adaptive speed control for permanent-magnet synchronous motor system with variations of load inertia," *IEEE Trans. Ind. Electron.*, vol. 56, no. 8, pp. 3050–3059, Aug. 2009.

[21] E. Sariyildiz, R. Oboe, and K. Ohnishi, "Disturbance observer-based robust control and its applications: 35th anniversary overview," *IEEE Trans. Ind. Electron.*, vol. 67, no. 3, pp. 2042–2053, Mar. 2020.

[22] Y. Li, Y. Hu, and W. Wu, "Complex-coefficient adaptive extended state observer for position estimation of PMSMs with enhanced robustness to disturbances," *IEEE J. Emerg. Sel. Top. Power Electron.*, vol. 13, no. 3, pp. 3324–3337, Jun. 2025.

[23] Y. Wang, Y. Jiao, H. Chen, and L. Yao, "Adaptive constraint control based peak-attenuated disturbance observer for the electric vehicle used permanent magnet synchronous motor," *Int. J. Elect. Power Energy Syst.*, vol. 166, 2025, Art. no. 110579.

[24] J. Sun, Z. Wang, S. Ding, J. Xia, and G. Xing, "Adaptive disturbance observer-based fixed time nonsingular terminal sliding mode control for path-tracking of unmanned agricultural tractors," *Biosyst. Eng.*, vol. 246, pp. 96–109, 2024.

[25] C. Song, W. Hu, J. Zhang, C. Zhao, and X. Sun, "A gain-adaptive high-order terminal sliding mode observer under SPMSM sensorless control," *IEEE Trans. Power Electron.*, vol. 40, no. 5, pp. 6555–6565, May 2025.

[26] X. Shen et al., "Fixed-time sliding mode control for NPC converters with improved disturbance rejection performance," *IEEE Trans. Ind. Inform.*, vol. 21, no. 6, pp. 4476–4487, Jun. 2025.

[27] X. Shen et al., "Sliding-mode control of neutral-point-clamped power converters with gain adaptation," *IEEE Trans. Power Electron.*, vol. 39, no. 8, pp. 9189–9201, Aug. 2024.

[28] S. Ding, W. Dou, J. Liu, J. Sun, and J. Yang, "Event-triggered adaptive super-twisting-like fractional control for path-tracking of autonomous agricultural vehicles," *IEEE/ASME Trans. Mechatron.*, early access, Sep. 12, 2025, doi: 10.1109/TMECH.2025.3603158.

[29] Z. Kang, X. Shen, Z. Liu, X. Liu, Y. Gao, and J. Liu, "Disturbance-tailored super-twisting control for NPC converters under unbalanced grid conditions," *IEEE Trans. Power Electron.*, vol. 41, no. 1, pp. 454–466, Jan. 2026.

[30] Y. Ma, T. Qin, and Y. Li, "Nonlinear extended state observer based super-twisting terminal sliding mode synchronous control for parallel drive systems," *IEEE/ASME Trans. Mechatron.*, vol. 28, no. 6, pp. 3087–3098, Dec. 2023.

[31] T. Zhang, Z. Xu, J. Li, H. Zhang, and C. Gerada, "A third-order super-twisting extended state observer for dynamic performance enhancement of sensorless IPMSM drives," *IEEE Trans. Ind. Electron.*, vol. 67, no. 7, pp. 5948–5958, Jul. 2020.

[32] J. Kim, S. Choi, and D. Yun, "Supercritical sliding-mode control for position tracking of PMSM with disturbance rejection," *IEEE Trans. Power Electron.*, vol. 41, no. 1, pp. 13–24, Jan. 2026.

[33] Y. Shtessel, M. Taleb, and F. Plestan, "A novel adaptive-gain supertwisting sliding mode controller: Methodology and application," *Automatica*, vol. 48, no. 5, pp. 759–769, 2012.

[34] G. Mohamed, A. A. Sofiane, and L. Nicolas, "Adaptive super twisting extended state observer based sliding mode control for diesel engine air path subject to matched and unmatched disturbance," *Math. Comput. Simul.*, vol. 151, pp. 111–130, 2018.

[35] R. Tafat, J. A. Moreno, and S. Streif, "Generalized super-twisting observer for a class of interconnected nonlinear systems with uncertainties," *IEEE Control Syst. Lett.*, vol. 9, pp. 793–798, 2025.

[36] X. Wang and S. Wang, "Fixed-time integral terminal sliding-mode control with super-twisting nonlinear extended-state observer for servo system with disturbances," *IEEE J. Emerg. Sel. Top. Ind. Electron.*, vol. 6, no. 1, pp. 435–446, Jan. 2025.

[37] Q. Hou, H. Wang, C. H. T. Lee, and S. Ding, "Composite adaptive super-twisting sliding mode control using barrier function for PM motor drives toward electric aircraft applications," *IEEE Trans. Power Electron.*, vol. 40, no. 11, pp. 16255–16264, Nov. 2025.

[38] H. Wu, C. Gan, H. Wang, S. Wang, R. Qu, and X. Liu, "Active disturbance rejection speed control with double-stage-ESO considering aperiodic and periodic disturbances for PMSM drives," *IEEE Trans. Ind. Electron.*, early access, Jan. 6, 2024, doi: 10.1109/TIE.2024.3519622.

[39] Q. Chen, Y. Li, Y. Hong, and H. Shi, "Prescribed-time robust repetitive learning control for PMSM servo systems," *IEEE Trans. Ind. Electron.*, vol. 71, no. 11, pp. 14753–14763, Nov. 2024.

[40] M. Tian, B. Wang, Y. Yu, Q. Dong, and D. Xu, "Enhanced one degree-of-freedom ADRC with sampled-data iterative learning controller for PMSM uncertain speed fluctuations suppression," *IEEE Trans. Transp. Electrific.*, vol. 10, no. 4, pp. 8321–8335, Dec. 2024.

[41] Z.-H. Liu, J. Nie, H.-L. Wei, L. Chen, F.-M. Wu, and M.-Y. Lv, "Second-order ESO-based current sensor fault-tolerant strategy for sensorless control of PMSM with b-phase current," *IEEE/ASME Trans. Mechatron.*, vol. 27, no. 6, pp. 5427–5438, Dec. 2022.

[42] W. Zhang, Y. Wang, M. Zeeshan, F. Han, and K. Song, "Super-twisting sliding mode control of grid-side inverters for wind power generation systems with parameter perturbation," *Int. J. Elect. Power Energy Syst.*, vol. 165, 2025, Art. no. 110501.

[43] S. Chang, Y. Wang, Z. Zuo, Z. Zhang, and H. Yang, "On fast finite-time extended state observer and its application to wheeled mobile robots," *Nonlinear Dyn.*, vol. 110, no. 2, pp. 1473–1485, 2022.

[44] T. Huo, X. Li, L. Zhu, and K. Wang, "Finite-time sliding mode adaptive control for unknown nonlinear beam system with neural network disturbance observer," *IEEE Trans. Autom. Sci. Eng.*, vol. 22, pp. 18281–18296, 2025.

[45] X. Liu, Y. Deng, H. Cao, J. Wang, H. Li, and C. H. T. Lee, "Modified ADRC based on quasi-resonant fixed-time-convergent extended state observer for PMSM current regulation," *IEEE Trans. Transp. Electrific.*, vol. 11, no. 1, pp. 1416–1430, Feb. 2025.

[46] B. Wang, M. Tian, Y. Yu, Q. Dong, and D. Xu, "Enhanced ADRC with quasi-resonant control for PMSM speed regulation considering aperiodic and periodic disturbances," *IEEE Trans. Transp. Electrific.*, vol. 8, no. 3, pp. 3568–3577, Sep. 2022.

[47] J. Liu, H. Li, and Y. Deng, "Torque ripple minimization of PMSM based on robust ILC via adaptive sliding mode control," *IEEE Trans. Power Electron.*, vol. 33, no. 4, pp. 3655–3671, Apr. 2018.

[48] L. Rosier, "Homogeneous Lyapunov function for homogeneous continuous vector field," *Syst. Control Lett.*, vol. 19, no. 6, pp. 467–473, 1992.

[49] K. Mei, Y. Gong, L. Ma, S. Ding, C. Ding, and Y. Yuan, "Design of integral-based HOSM controller under perturbations of unknown yearmagnitudes," *IEEE Trans. Cybern.*, vol. 55, no. 9, pp. 4103–4113, Sep. 2025.

[50] C. Qian and J. Li, "Global output feedback stabilization of upper-triangular nonlinear systems using a homogeneous domination approach," *Int. J. Robust Nonlinear Control*, vol. 16, no. 9, pp. 441–463, 2006.

[51] Q. Hou and S. Ding, "GPIO based super-twisting sliding mode control for PMSM," *IEEE Trans. Circuits Syst. II, Exp. Briefs*, vol. 68, no. 2, pp. 747–751, Feb. 2021.

[52] J. Sun, Z. Pu, J. Yi, and Z. Liu, "Fixed-time control with uncertainty and measurement noise suppression for hypersonic vehicles via augmented sliding mode observers," *IEEE Trans. Ind. Inform.*, vol. 16, no. 2, pp. 1192–1203, Feb. 2020.

[53] W. Dong, J. A. Farrell, M. M. Polycarpou, V. Djapic, and M. Sharma, "Command filtered adaptive backstepping," *IEEE Trans. Control Syst. Technol.*, vol. 20, no. 3, pp. 566–580, May 2012.

[54] H. Du, C. Qian, S. Yang, and S. Li, "Recursive design of finite-time convergent observers for a class of time-varying nonlinear systems," *Automatica*, vol. 49, no. 2, pp. 601–609, 2013.

[55] Q. Hou, H. Wang, C. Zhao, and C. H. T. Lee, "Super-twisting extended state observer-based quasi-proportional-resonant controller for permanent magnet synchronous motor drive system," *IEEE Trans. Transp. Electrific.*, vol. 10, no. 1, pp. 1596–1604, Mar. 2024.

[56] C. Xia, B. Ji, and Y. Yan, "Smooth speed control for low-speed high-torque permanent-magnet synchronous motor using proportional–integral–resonant controller," *IEEE Trans. Ind. Electron.*, vol. 62, no. 4, pp. 2123–2134, Apr. 2015.

[57] Y. Cui, Z. Yin, P. Luo, D. Yuan, and J. Liu, "Linear active disturbance rejection control of IPMSM based on quasi-proportional resonance and disturbance differential compensation linear extended state observer," *IEEE Trans. Ind. Electron.*, vol. 71, no. 10, pp. 11910–11924, Oct. 2024.

[58] L. Chen et al.., "Sensorless fixed-time sliding mode control of PMSM based on barrier function adaptive super-twisting observer," *IEEE Trans. Power Electron.*, vol. 39, no. 3, pp. 3037–3051, Mar. 2024.

Jinlin Sun (Member, IEEE) received the B.Eng. degree in automation from Jiangsu University, Zhenjiang, China, in 2016, and the Ph.D. degree in control theory and control engineering from the Institute of Automation, Chinese Academy of Sciences, Beijing, China, in 2021.

From 2019 to 2020, he visited the Department of Electrical, Computer, and Biomedical Engineering, University of Rhode Island, South Kingstown, RI, USA. He is currently an Associate Professor with the School of Electrical and Information Engineering, Jiangsu University. His research interests include autonomous vehicles and antidisturbance control.

Dr. Sun was the recipient of the Excellent Ph.D. Dissertation Award from the Chinese Association of Automation (CAA) in 2022, and was selected for the Young Elite Scientists Sponsorship Program by China Association for Science and Technology (CAST) in 2024.

Nengwen Zhu was born in Anhui, China, in 1996. He is currently working toward the M.S. degree in control engineering with the School of Electrical and Information Engineering, Jiangsu University, Zhenjiang, China.

His research interests include nonlinear control, disturbance rejection, and applications to permanent magnet synchronous motor systems.

Qiankang Hou received the B.Eng. degree in electrical engineering and the Ph.D. degree in control science and engineering from Jiangsu University, Zhenjiang, China, in 2017 and 2023, respectively.

Since 2023, he has been with Changzhou University, Changzhou, China, where he is currently a Lecturer with the School of Mechanical Engineering. From 2021 to 2022, he visited the School of Electrical and Electronic Engineering, Nanyang Technological University, Singapore. His research interests include power electronics, electric machines and drives, and advanced control strategies.

Shihong Ding (Senior Member, IEEE) received the B.E. degree in mathematics from Anhui Normal University, Wuhu, China, in 2004, and the M.S. and Ph.D. degrees in automatic control from Southeast University, Nanjing, China, in 2007 and 2010, respectively.

From 2008 to 2009, during the graduate studies, he visited The University of Texas at San Antonio, San Antonio, TX, USA. After graduation, he held a research fellowship with the University of Western Sydney, Sydney, NSW, Australia, for one year. He also visited Yeungnam University, Gyeongsan, South Korea, from July 2018 to August 2018 and RMIT University, Melbourne, VIC, Australia, from 2019 to 2020 and 2024 to 2025, respectively. Since 2010, he has been with the School of Electrical and Information Engineering, Jiangsu University, Zhenjiang, China, where he is currently a Full Professor. His research interests include smart agricultural machinery and sliding mode control.

Dr. Ding is currently an Associate Editor for IEEE TRANSACTIONS ON INDUSTRIAL ELECTRONICS and *International Journal of Adaptive Control and Signal Processing*, as well as a Subject Editor for *Nonlinear Dynamics*.

Jun Yang (Fellow, IEEE) received the B.Sc. degree in automation from the Department of Automatic Control, Northeastern University, Shenyang, China, in 2006, and the Ph.D. degree in control theory and control engineering from the School of Automation, Southeast University, Nanjing, China, in 2011.

In 2020, he joined the Department of Aeronautical and Automotive Engineering, Loughborough University, as a Senior Lecturer, and was promoted to a Reader, in 2023. His research interests include disturbance observer, motion control, visual servoing, nonlinear control, and autonomous systems.

Dr. Yang is an Associate Editor or Technical Editor for IEEE TRANSACTIONS ON INDUSTRIAL ELECTRONICS, IEEE/ASME TRANSACTIONS ON MECHATRONICS, IEEE OPEN JOURNAL OF THE INDUSTRIAL ELECTRONICS SOCIETY, etc. He was the recipient of the EPSRC New Investigator Award. He is a Fellow of IET and AAIA.